Continuous dimer angles on the silicon surface: Critical properties and the Kibble-Zurek mechanism

Andreas Weitzel,[1,*] Gernot Schaller,[1] Friedemann Queisser,[1] and Ralf Schützhold[1,2]
[1]*Helmholtz-Zentrum Dresden-Rossendorf, Bautzner Landstraße 400, 01328 Dresden, Germany*
[2]*Institut für Theoretische Physik, Technische Universität Dresden, 01062 Dresden, Germany*

(Received 9 September 2024; revised 18 November 2024; accepted 22 November 2024; published 12 December 2024)

Langevin dynamics simulations are used to analyze the static and dynamic properties of an XY model adapted to dimers forming on Si(001) surfaces. The numerics utilize high-performance parallel computation methods on GPUs. The static exponent ν of the symmetry-broken XY model is determined to $\nu = 1.04$. The dynamic critical exponent z is determined to $z = 2.13$ and, together with ν, shows the behavior of the Ising universality class. For time-dependent temperatures, we observe frozen domains and compare their size distribution with predictions from Kibble-Zurek theory. We determine a significantly larger quench exponent that shows little dependence on the damping or the symmetry-breaking field.

DOI: 10.1103/PhysRevB.110.245125

I. INTRODUCTION

In the area of semiconductor technology, silicon has become the cornerstone material driving the innovations that power our modern world in the *Silicon Age* [1]. The Si(001) surface of monocrystalline silicon is particularly relevant as it forms an interface with the oxide layer in transistors that isolates silicon nanowires from their environment. While static properties of Si(001), e.g., surface configurations, their energies, and electronic structures, are thoroughly investigated by theoretical [2–6] and experimental [7–11] works, the dynamic properties [12] are not yet well understood. The surface undergoes a continuous order-disorder phase transition with Ising critical exponents [9] between two surface patterns [13], leading to striking dynamic behavior at the critical point. A phenomenon exhibiting rich dynamics is the Kibble-Zurek mechanism (KZM) [12,14–25], which describes the unavoidable nonadiabatic (deviating from instantaneous equilibrium) evolution of systems as they cross phase boundaries. When crossing from a disordered to an ordered phase, the velocity at which systems undergo this transition is directly related to the size of ordered domains (see Fig. 1), which in turn influences the semiconducting properties [26–28] of the surface.

The Si(001) surface has often been mapped onto the discrete two-dimensional Ising model [3–5,9]. In this paper, a continuous model of the surface buckling is developed and numerically investigated by Langevin dynamics [29,30] simulations. The emphasis will be put on differences of the dynamics between discrete simulations using the Ising model—for which a scaling matching the predictions by KZM has been observed [12,31]—and continuous modeling using an adapted classical XY model [32–36].

This paper is organized as follows: In Sec. II, the theory of critical scaling for the static and dynamic case, as well as the Kibble-Zurek scenario, is laid out. The used model and its mapping to the Si(001) surface are described in Sec. III. The results for the static and dynamic critical properties are discussed in Sec. IV. We conclude our findings in Sec. V and provide technical details in the Appendixes.

II. THEORETICAL BACKGROUND

A. Static scaling

Observables of systems near a phase boundary obey universal static scaling laws in the thermodynamic limit. They describe the power-law dependence of system quantities in equilibrium on control parameters like the temperature T close to the critical point. For example, the correlation length ξ depends on the reduced temperature

$$\varepsilon = \frac{T - T_c}{T_c} \tag{1}$$

via

$$\xi(\varepsilon) = \xi^{\pm}\varepsilon^{-\nu}, \tag{2}$$

showing a divergence at the critical value $T = T_c$ with the *critical exponent* $\nu > 0$. This behavior is shared by all systems undergoing a second-order phase transition [37,38] and is independent of the concrete microscopic properties. The static critical exponent ν assumes a universal value for systems that share fundamental properties like symmetries or their dimensionality. Systems that possess the same set of critical exponents are said to belong to the same *universality class*. In contrast, the *critical amplitudes* $\xi^{\pm}$ are nonuniversal and vary according to the microscopics. The superscript $\pm$ denotes whether the phase transition is approached from below $(-)$ or above $(+)$ the critical temperature.

*Contact author: a.weitzel@hzdr.de

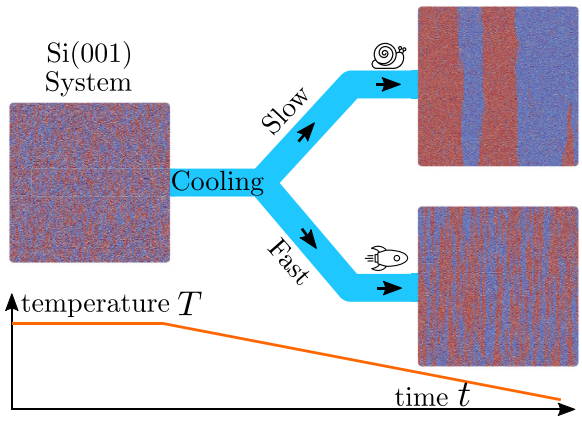

FIG. 1. A representation of the silicon (001) surface with the colors mapping into the continuous dimer buckling angle is shown. The system is cooled down with a varying rate. The cooling rate determines the size of ordered patches after the quench.

B. Dynamic scaling

In contrast to static scaling, *dynamic scaling* describes the behavior of the relaxation time τ across the transition. The relaxation time quantifies the time required for fluctuations in the system on the largest lengthscale to equilibrate. Near the critical point, it depends on the correlation length as [39]

$$\tau = \tau_\xi \xi^z(\varepsilon) = \tau_\varepsilon^\pm \varepsilon^{-\nu z}, \tag{3}$$

defining the universal *dynamic critical exponent* z, the critical amplitude τ_ξ, as well as $\tau_\varepsilon^\pm := \tau_\xi (\xi^\pm)^z$. Just as the correlation length, the relaxation time becomes infinite at the critical point. This phenomenon is commonly referred to as *critical slowing down* [37,39,40] and describes the inability of thermodynamic systems to equilibrate at $\varepsilon = 0$.

The Kibble-Zurek mechanism [12,14–19] deals with the question of how this nonadiabatic evolution influences the system observables after a quench through the critical point. A simple quench is a decrease of the reduced temperature (1) linear in time t following

$$\varepsilon(t) = -\frac{t}{\tau_Q}, \tag{4}$$

with the *quench timescale* τ_Q. The main statement of the KZM argument is that system quantities after the quench, like ξ, are directly proportional to their values $\hat{\xi}$ at the *freezeout point* defined by

$$\tau(\hat{t}) = \hat{t}, \tag{5}$$

after which the system equilibration can no longer follow the driving. When approaching the transition point from the high-temperature phase, combining Eqs. (3)–(5) yields the scaling of the frozen correlation length

$$\hat{\xi} = \xi(\varepsilon(\hat{t})) = \xi^+ / |\varepsilon(\hat{t})|^\nu = \xi^+ \left| \frac{\tau_Q}{\tau_\varepsilon^+} \right|^{\mu_{\mathrm{KZM}}}, \tag{6}$$

with

$$\mu_{\mathrm{KZM}} = \frac{\nu}{1 + \nu z} \tag{7}$$

being the *quench exponent* according to KZM. Equation (6) quantifies the dependence of the quenched correlation length on the quench timescale τ_Q. A specialty of the KZM argument is that it enables us to predict the behavior of quenched systems solely from universal exponents.

III. MODEL

The upcoming investigations will make use of molecular-dynamics (MD) [30], or more precisely, *Langevin dynamics* simulations [29]. MD simulations numerically solve Newton's equations of motion to describe the behavior of many-particle systems, thus going beyond a discrete modeling of the dimers, which omits the details of the dynamics. Therefore, it is desirable to investigate whether a simulation with a continuum of states results in other dynamic critical behavior than the discrete models. Below, we first introduce a model similar to the Ising model that offers continuous states and reproduces the experimentally observed Ising static critical exponents, and we explain its relation to the silicon surface as well as its numerical Langevin dynamics simulation.

A. Classical XY model

The classical two-dimensional XY model (or planar rotor model) without symmetry-breaking fields is characterized by sites each hosting a unit-length rotor in two dimensions $\vec{s} = (\cos(\vartheta), \sin(\vartheta))$, with $\vartheta \in [0, 2\pi)$ characterizing the angle of the in-plane rotors. Its nearest-neighbor Hamiltonian on a lattice with sites (i, j) is given by

$$\tilde{H}_{XY} = -J_\parallel \sum_{ij} \vec{s}_{i,j} \cdot \vec{s}_{i+1,j} - J_\perp \sum_{ij} \vec{s}_{i,j} \cdot \vec{s}_{i,j+1}, \tag{8}$$

with the coupling constants J_δ and $\delta \in \{\perp, \parallel\}$. In contrast to the two-dimensional Ising model [41,42], an exact closed solution to the two-dimensional XY model is unknown. However, it has been studied in numerous analytical [32–36] and numerical [43–45] works. Without symmetry-breaking fields, it does not exhibit an ordinary phase transition with universal critical exponents, but undergoes the Kosterlitz-Thouless transition [33]. In this case, the system transitions from an unordered state to a quasiordered state of vortex-antivortex pairs. The correlation length still diverges, but does not follow Eq. (2) anymore. Instead, when approaching the transition from the disordered state, ξ diverges exponentially and, in the ordered state, the spin-spin correlations vary continuously with the temperature [46].

The quantum version of Eq. (8) can be obtained by replacing the spins with Pauli matrices [47]. It is relevant for insulator to superfluid quantum transitions [48], effective interactions between quantum dots [49], the quantum-Hall effect [50], as well as cavity QED systems in quantum computers [50]. In two dimensions, it also undergoes a Kosterlitz-Thouless transition [51,52], like its classical counterpart.

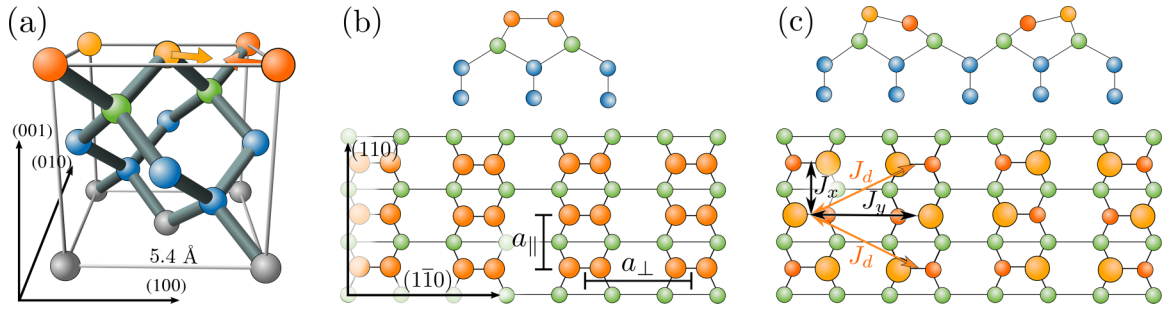

FIG. 2. The figure, inspired by [9], shows the crystal structure of silicon and two surface configurations. The coloring of the silicon atoms corresponds between (a) and (b),(c). In the following, the surfaces are addressed using Wood's notation for overlayers [55]. (a) The crystalline structure of Si in its solid state is shown [56]. The orange silicon atoms dimerize during reconstruction of the (001) surface. The coordinate axes are denoted by their Miller indices and normal to their corresponding crystallographic planes. In (b) and (c), Si(001) surface patterns are shown from a side and top-down perspective. In the top-down view, silicon atoms that are closer to the reader are magnified. (b) The formation of dimers results in the symmetric $p(2 \times 1)$ reconstruction and reduces the energies by 1.8 eV per dimer compared to the nondimerized structure. (c) The dimers are unstable to vertical buckling. The buckling pattern that was found to have the lowest surface energy is the $c(4 \times 2)$ reconstruction. The fundamental couplings J_δ, $\delta \in \{x, y, d\}$ are indicated by arrows.

We generalize Hamiltonian (8) by a p-fold symmetry-breaking field of strength h as well as a multiplying factor q (similar to the generalized XY model [53]) to obtain

$$\begin{aligned} H_{XY} = &- J_\parallel \sum_{i,j} \cos(q(\vartheta_{i,j} - \vartheta_{i+1,j})) \\ &- J_\perp \sum_{i,j} \cos(q(\vartheta_{i,j} - \vartheta_{i,j+1})) \\ &+ h \sum_{i,j} \cos(p\vartheta_{i,j}). \end{aligned} \tag{9}$$

The purpose of q is to enable state-space restrictions. The critical properties change drastically if a symmetry-breaking field is introduced. In this case, José *et al.* [34] showed by renormalization-group calculations that the transition changes to the universality class of the p-state clock model or the vector Potts model [54]. The determining factor for the specified universality is the number of minima of the symmetry-breaking term. The case $p = 2$ yields the Ising transition for any nonzero h.

B. The Si(001) surface

Silicon crystallizes in a diamond cubic structure, as shown in Fig. 2(a). When cutting this crystal structure along the crystallographic (001) plane, the resulting surface reconstructs by dimerization of the surface atoms [57] [see Fig. 2(b)]. The bonding lowers the surface energy by roughly 1.8 eV per dimer [2,58,59]. The dimers can further reduce their energy by buckling vertically. They tilt to an angle of about 18° with the surface plane [2,3], which lowers the surface energy by another 0.15 eV [4] per dimer. A charge transfer of approximately $0.1e$ [9,60] is induced by the buckling.

Theoretical [2–4,9] and experimental (low-energy electron diffraction [7–9] and scanning tunneling microscopy [10,11]) investigations have found the $c(4 \times 2)$ reconstruction, shown in Fig. 2(c), to be the lowest-energy geometry. It minimizes the interaction energy as well as the surface stress [3]. The alternating buckling in both directions suggests an antiferromagnetic interaction along both directions. However, apart from an antiferromagnetic interaction along the dimer rows, experimental observations [9,61] actually indicate ferromagnetic transverse couplings $J_y > 0$ and

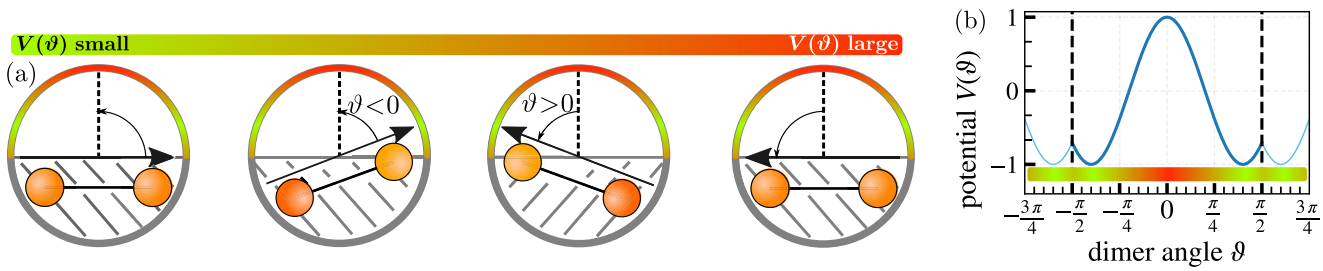

FIG. 3. (a) Unit circles are shown as visualizations of the state space. The colored part of the unit circle represents the allowed states. The states are depicted as arrows inside the unit circle. The buckling angles of the silicon dimers are mapped to the rotors of the XY model. Since the silicon atoms are indistinguishable, a rotation by π maps to the same state. Hence, the state space is only half the unit circle. The coloring of the allowed states corresponds to the value of the potential $V(\vartheta)$. The vertical dimer position is highly unlikely, and the minimum of the potential is roughly located at the equilibrium buckling angles of the dimers. Note that the left and right vectors are the same state and one of them is excluded by defining $\vartheta \in [-\pi/2, \pi/2)$. (b) The on-site potential is shown in dependence of the dimer angle. The allowed phase space is delimited by vertical dashed lines. Outside the allowed states, the angles are mapped back to $\vartheta \in [-\pi/2, \pi/2)$ by modulo operation. The periodic continuation of the potential is indicated by the light blue line.

additional ferromagnetic diagonal couplings $J_d > 0$. The dimer interactions are strongly anisotropic, with $|J_x|$ being much larger than $|J_y|$, enforcing alternating buckling in the (110) direction. The ferromagnetic diagonal interactions J_d overpower J_y, so that diagonal alignment is preferred, which in turn implies antialignment in the $(1\bar{1}0)$ direction, so that the effective transverse coupling is also antiferromagnetic. Because of the strong anisotropy, it is satisfactory to consider only effective nearest-neighbor couplings, which enables us to absorb the diagonal interactions J_d into an effective transverse

$$J_\perp = J_y - 2J_d < 0 \tag{10}$$

across the dimer rows [61]. The effective coupling along the dimer rows remains antiferromagnetic, $J_\parallel = J_x$.

The silicon (001) surface exhibits an order-disorder phase transition from the disordered $p(2 \times 1)$ phase [Fig. 2(b)] to the ordered $c(4 \times 2)$ reconstruction [Fig. 2(c)] at a critical temperature of about $T_c \approx 200$ K [13,61]. The $p(2 \times 1)$ structure is short term for the disordered phase since fast flipping of the dimers at a rate of about 10^{11} Hz [59] lets the system appear to be in the $p(2 \times 1)$ state at high-temperature measurements. This continuous phase transition will be of central importance in the following discussion.

Below T_c, the strong anisotropy leads to long streaks of order along the dimer rows and short domains of order across the dimer rows. The correlation length amplitude in parallel direction $\xi_\parallel^+$ is larger than the transverse amplitude $\xi_\perp^+$ by a factor of 5 [61]. In units of the lattice constants $a_\parallel$ and $a_\perp$ [see Fig. 2(b)], this implies $(\xi_\parallel^+/a_\parallel)/(\xi_\perp^+/a_\perp) \approx 10$.

Si(001) was mapped onto the exactly solvable two-dimensional Ising model in previous research [3–5,12,61] by assigning its two discrete states to the two equilibrium buckling angles of the dimers. A good agreement between the experimentally measured static critical properties of the surface's phase transition and the Ising universality class has been found [9,61]. Furthermore, simulations based on kinetic Monte Carlo methods [62] have revealed a quench scaling that roughly matches the KZM [12].

C. Mapping the *XY* model to Si(001)

The natural choice of mapping the Si(001) dimers to the *XY* model is to identify the dimer buckling angles with the rotor angles ϑ. Since silicon atoms are indistinguishable, a rotation of the dimer by π results in the same state. We will therefore restrict the state space of the rotor to $\vartheta \in [-\pi/2, \pi/2)$. To ensure that the interaction terms in Eq. (9) have the same periodicity as ϑ, we set $q = 2$ inside the cosine terms. The correspondence between the rotors and the dimers is depicted in Fig. 3. The parameter p in Eq. (9) determines the number of minima of the on-site potential and thereby the equilibrium position of the dimers. As we have cut the state space in half, the effective integer p_{eff} relevant for the clock model classification of Sec. III A will be $p_{\text{eff}} = \lceil p/2 \rceil$. Since the dimers have two equilibrium buckling angles $\vartheta_\pm$, we demand $2 < p \leqslant 4$, corresponding to an effective $p_{\text{eff}} = 2$. Due to the additional antiferromagnetic interaction, the equilibrium position of the dimers will be somewhere between the minima of the symmetry-breaking potential and $\pm\pi/4 \leqslant \vartheta_\pm$. Since the upcoming investigations will not involve quantitative predictions but rather an assessment of universal behavior, we will set $p = 2.5$ and leave the exact calibration of equilibrium buckling angles with experimental data to future work.

D. Langevin dynamics

A molecular-dynamics approach solving the equations of motion for every dimer will be employed to numerically investigate the adapted *XY* model. The Si(001) surface is thermally coupled to the silicon bulk, which acts as a thermal reservoir. One way to model thermalization with this reservoir, even for interacting particle potentials, is to replace Newton's equations of motion with Langevin equations. In other words, the movements of the dimers will be modeled as Brownian motion in a (double-well) potential. Since we want to describe the full dynamics of the silicon dimers in terms of the buckling angle, we add the kinetic energy to the Hamiltonian of Eq. (9), reading

$$H = \sum_{i,j} \frac{1}{2} I \omega_{i,j}^2 + H_{XY}, \tag{11}$$

with the dimer moment of inertia I and the angular velocity $\omega_{i,j}$.

In the following, we will work with a dimensionless representation of the problem, meaning that all quantities, including time t or angular velocity ω, will be given in multiples of I or I^{-1}, respectively.

The dimensionless stochastic equations of motion for rotary motion in a (periodic) potential $V(\{\vartheta\})$ are, in units of I, given by [29,63]

$$\begin{aligned} \frac{\mathrm{d}}{\mathrm{d}t}\vartheta_{i,j}(t) &= \omega_{i,j}(t), \\ \frac{\mathrm{d}}{\mathrm{d}t}\omega_{i,j}(t) &= -\eta\omega_{i,j}(t) - \frac{\partial V(\{\vartheta\})}{\partial \vartheta_{i,j}} + \sqrt{2\eta T}\,\Gamma(t), \end{aligned} \tag{12}$$

with the *damping* η, temperature T, and the *Gaussian white noise process* $\Gamma(t)$ [29]. The latter satisfies

$$\langle \Gamma(t) \rangle = 0 \qquad \text{and} \qquad \big\langle \Gamma(t)\Gamma(t+t') \big\rangle = \delta(t'). \tag{13}$$

To evaluate the on-site potential, we map the angles back to the allowed interval $\vartheta_{i,j} \in [-\pi/2, \pi/2)$ by modulo operation after every integration step. The simulation is implemented in CUDA C++ [64] using Thrust [65] as a high-level interface. The integration scheme is described in Appendix A 1. We have benchmarked the thermalization of this system for dimer pairs in Appendix A 2. Additionally, the dynamics of Brownian motion in a harmonic potential and the used integration step size dt have been tested.

IV. RESULTS

The simulations have been performed with a coupling constant ratio of $J_\parallel/J_\perp = 100$ as the numerics have shown that this choice reproduces the experimental equilibrium correlation length ratio [61] of $(\xi_\parallel^+/a_\parallel)/(\xi_\perp^+/a_\perp) \approx 10$. To keep all values around unity, $IJ_\parallel = 10$ and $IJ_\perp = 0.1$ are chosen. Unless marked otherwise, the damping is set to $\eta = 1$. The damping does not influence the static properties of the system, and the effects on the dynamics are investigated later. Since

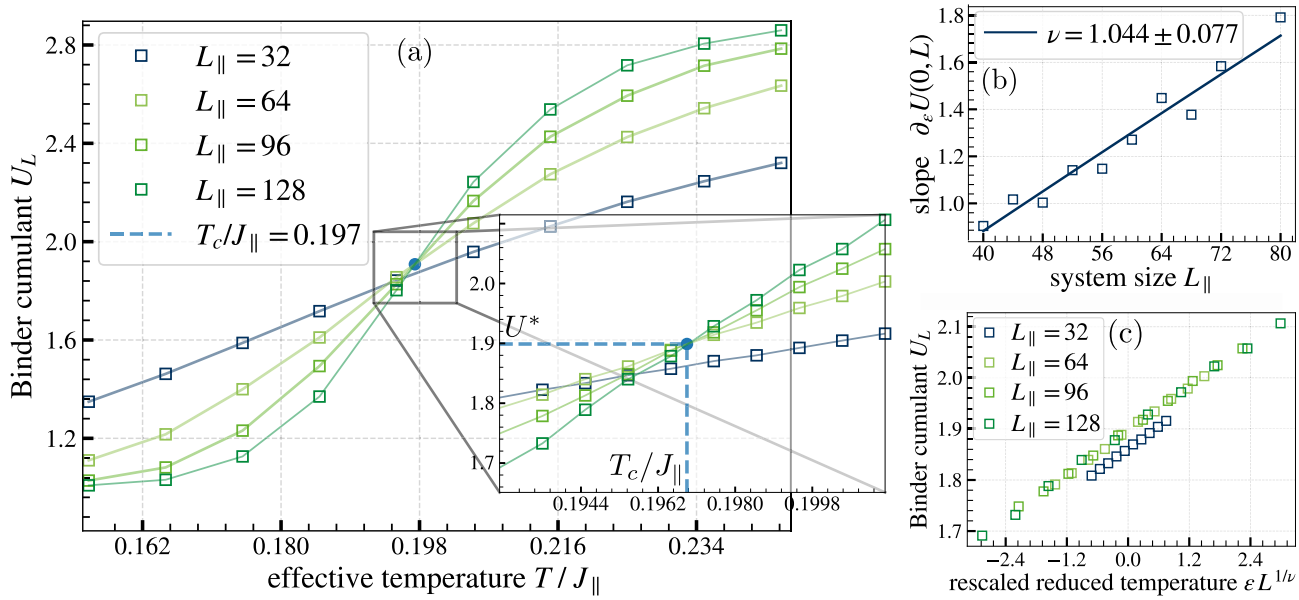

FIG. 4. (a) The results of $U(\varepsilon, L)$ for selected sizes L are computed close to the critical point. The systems were initialized in a totally ordered state with $U(0, L) = 1$ as it minimizes the time of relaxation to $U(\varepsilon, L)$ [66]. Except for the smallest $L = 32$, all cumulants intersect approximately at the same point $(\beta_c J_\parallel)^{-1} = 0.197$. (b) The derivatives $\partial_\varepsilon U(\varepsilon, L) \propto L^{1/\nu}$ are shown in dependence of the system size. They are calculated using a standard central difference method including, among others, the data points of (a). The fitting yields $\nu = 1.04 \pm 0.08$ (fit uncertainty [67]), which is in good accordance with the Ising model. (c) Close to the critical point, the Binder cumulant for different system sizes collapses on a line if plotted vs $\varepsilon L^{1/\nu}$, as expected from Eq. (17). Corrections to FSS are again visible for $L = 32$.

the energy barrier between the equilibrium positions is proportional to h, the magnitude of h slows down the dynamics of the system significantly. As the computational resources are limited, the selected value of h is not fitted to the experimental system but set to $Ih = I\sqrt{J_\perp J_\parallel} = 1$.

A. Static scaling

Since some modifications have been made to the anisotropic XY model, e.g., restricting the state space and using rational p instead of the integer values used in [34], it is desirable to verify that the model still belongs to the expected Ising universality class. We therefore start by extracting the static critical exponent ν. The solution of the equations of motion is computationally expensive, so finite-size scaling (FSS) methods [37,68] will be employed. More specifically, we will make use of the FSS of the Binder cumulant [69] defined by

$$U(\varepsilon, L) = \frac{\langle M^4(L)\rangle_\varepsilon}{\langle M^2(L)\rangle_\varepsilon^2}, \tag{14}$$

with the ensemble average $\langle\cdot\rangle_\varepsilon$ at reduced temperature ε, and $M(L)$ being the lattice average

$$M(L) = \frac{1}{N(L)} \sum_{i=0}^{N(L)} s_i \tag{15}$$

of a system of size L with $N(L)$ lattice sites, e.g., $N(L) = L^2$ for a two-dimensional quadratic lattice. In our adapted XY model, the site's state s_i is characterized by $s_i(\vartheta_i) = \sin(q\vartheta_i)$ with $q = 2$ so that our order parameter is analogous to the magnetization in the x-direction in the model with full state space $M_x = \langle \sin(\vartheta_i)\rangle$. Additionally, the factor 2 enforces the π-periodicity of our model and roughly maps the equilibrium buckling angles $\vartheta_\pm$ to $\sin(2\vartheta_\pm) \approx \pm 1$, like in the Ising model. The finite-size scaling of $U(\varepsilon, L)$ can be parametrized [38,70] as

$$U(\varepsilon, L) = U^* + A\varepsilon L^{1/\nu}\left(1 + BL^{-\tilde{\omega}} + \cdots\right), \tag{16}$$

with $\tilde{\omega}$ being the smallest irrelevant exponent in renormalization-group language [37,38]. The symbols A and B are unknown proportionality constants. The curves $U(\varepsilon, L)$ intersect for different system sizes L at $U(0, L) = U^*$. For Ising lattices where $s_i = \sigma_i$, $\sigma_i \in \{-1, 1\}$, and thus M is the magnetization per spin, it can be shown that the Binder cumulant jumps from its zero-temperature limit $U(\varepsilon < 0, \infty) = 1$ below the critical temperature to its infinite-temperature limit $U(\varepsilon > 0, \infty) = 3$ above the critical temperature [69]. Although the Binder cumulant U depends on factors like boundary conditions, lattice shapes, and anisotropies [71], the intersection remains at T_c regardless of these factors and can therefore be used to extract the critical temperature. The preceding implications can be generalized to spin dimensionalities larger than 1 [72] and have been shown to be consistent with the XY model [73–75]. By simulating systems around the critical point and computing $\partial_\varepsilon U(\varepsilon, L)$ at $\varepsilon = 0$, the exponent ν may then also be calculated by fitting

$$\ln\left(\left.\frac{\partial U(\varepsilon, L)}{\partial \varepsilon}\right|_{\varepsilon=0}\right) \approx \ln\left(AL^{1/\nu}\right) = \ln(A) + \frac{1}{\nu}\ln(L) \tag{17}$$

and extracting the slope $1/\nu$. Figure 4 shows excellent agreement with the Ising critical exponent $\nu = 1$. The evaluation and assessment of the simulation is described in Appendix B .

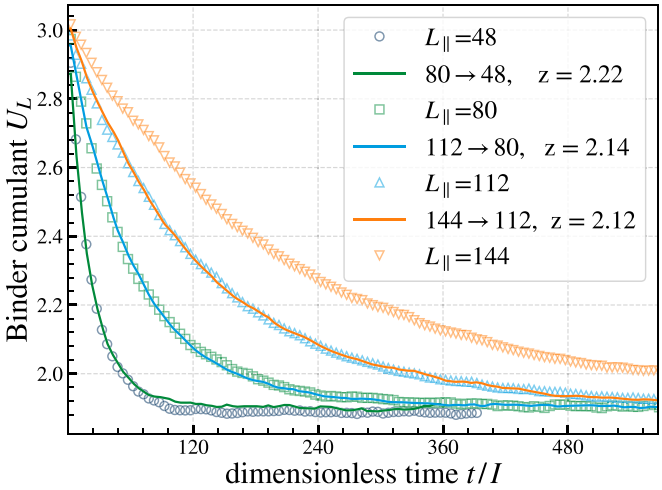

FIG. 5. The relaxation of the Binder cumulant is shown vs the dimensionless time for selected sizes L. The dynamic critical exponent z can be extracted by finding a time rescaling factor $b^{-z} = (L_1/L_2)^{-z}$ such that $U(t, \varepsilon, L_1)$ and $U(b^{-z}t, \varepsilon, L_2)$ overlap. The best rescaling of $U(t, \varepsilon, L_1) \to U(t, \varepsilon, L_2)$ is selected by rasterizing z in steps of 0.01 and minimizing the squared error between the interpolated curves. The rescalings $144 \to 112$ and $112 \to 80$ yield an average exponent of $z = 2.13$, which is very close to the Ising universality class $z = 2.16$ (see Appendix E).

B. Dynamic scaling

Additionally, the Binder cumulant is useful to extract the dynamic critical exponent z. We employ the cumulant relaxation method introduced by Li *et al.* in [76] and extend the cumulant by a time dependence $U(\varepsilon, L) \to U(t, \varepsilon, L)$. Their argument exploits that a totally unordered system at $U(0, \infty, L) = 3$ coupled to a reservoir at $\varepsilon = 0$ relaxes to its equilibrium value $U(\infty, 0, L) = U^*$. The timescale at which this relaxation happens increases with the system size. Quantitatively, it can be shown that the time-resolved behavior of systems of different sizes L_1 and L_2 can be formulated as [76]

$$U(t, 0, L_1) = U(b^{-z}t, 0, L_2), \tag{18}$$

with $b = L_1/L_2$ being the spatial rescaling factor. The dynamic exponent can be extracted by finding a temporal rescaling factor b^{-z} so that the relaxation curves for different sizes L_i collapse. Since this only holds precisely for the critical relaxation, the critical temperature of the system has to be determined beforehand by using the intersection in Fig. 4(a). The exponent z has then been calculated by minimizing the squared deviation between rescaled curves for a discrete rasterization of z-values with a step size of 0.01. Fig. 5 shows that the extracted z is very close to the best guess of the Ising z in Table I. Hence, we believe that our model still belongs to the Ising universality class.

C. Quenches

We introduce the general quench exponent μ_Q by the scaling of the quenched correlation length ξ with the quench timescale τ_Q,

$$\xi \propto \tau_Q^{\mu_Q}. \tag{19}$$

TABLE I. Recent results for the dynamic critical exponent z are summarized. The estimates are obtained by Monte-Carlo methods (MC) [77], renormalization-group calculations (RG) [78,79], and high-temperature expansion (HT) [80].

Source	Method	Result
[77]	MC	2.167
[78]	RG	2.14 ± 0.02
[79]	RG	2.183 ± 0.005
[80]	HT	2.15
z_{Ising}	Average	2.16

The KZM has been verified in numerous experimental [17–19] and numerical [12,20,21] investigations. Hence, we expect a value of $\mu_Q = \mu_{\text{KZM}} \approx 0.32$ from previous simulations. We will examine linear quenches like that described by Eq. (4) for a temperature range symmetric around the critical point,

$$\varepsilon_i = -\varepsilon_f, \tag{20}$$

so that the absolute values of the initial temperature ε_i and the final temperature ε_f match. The simulation is stopped right after ε_f is reached, so there is no after-quench equilibration phase. Figure 6 shows the time-resolved quench process in terms of the parallel correlation length $\xi_\parallel(t)$. The absolute value $|\varepsilon_i| = |\varepsilon_f|$ is chosen so that the evolution at the beginning of the quench is approximately adiabatic, meaning the orange equilibrium curve and the dynamic path in Fig. 6 overlap. At discrete time points, the state of the quenched ensemble is represented by a section snapshot of a quenched system at the corresponding time. The results of the quenches at different timescales are shown in dark blue in Fig. 7. The calculation of the correlation length is described in Appendix C. The system sizes are chosen so that the frozen correlation length is smaller than $L_\delta/10$. The extracted quench exponent for $\eta = h = 1$ of $\mu_Q \approx 0.47$ deviates strongly from the expected value μ_{KZM}. Since the parameters h and η have been observed to influence the dynamics drastically, it might be worthwhile to observe their influence on the quench exponent. This is investigated by the other curves in Fig. 7. Large η as well as large h slow down the dynamics of the quench and result in the linear scaling region of ξ moving toward slower quenches. The slope of the scaling region, however, shows, except for small η, no sensitive dependence on both parameters. Small η reveal the existence of a bump in the $\xi(\tau_Q)$ curve. This might be due to a retardation effect between the controlled reservoir temperature and the state of the system, which is influenced also by the kinetic energy of the dimers. The rotation of the dimers decays slower for small η and therefore the system keeps a larger energy per degree of freedom for a longer time. This might lead to the effect that quickly quenched underdamped systems are dominated by the rotational energy. For fast quenches, no significant change in the average dimer energy has happened until the end of the quench. As the quench timescale becomes larger, rotation is damped and the usual mechanisms take over rapidly. With the current results, a dependence of μ_Q on the quantitative values of h or η is improbable. Hence, averaging the quench

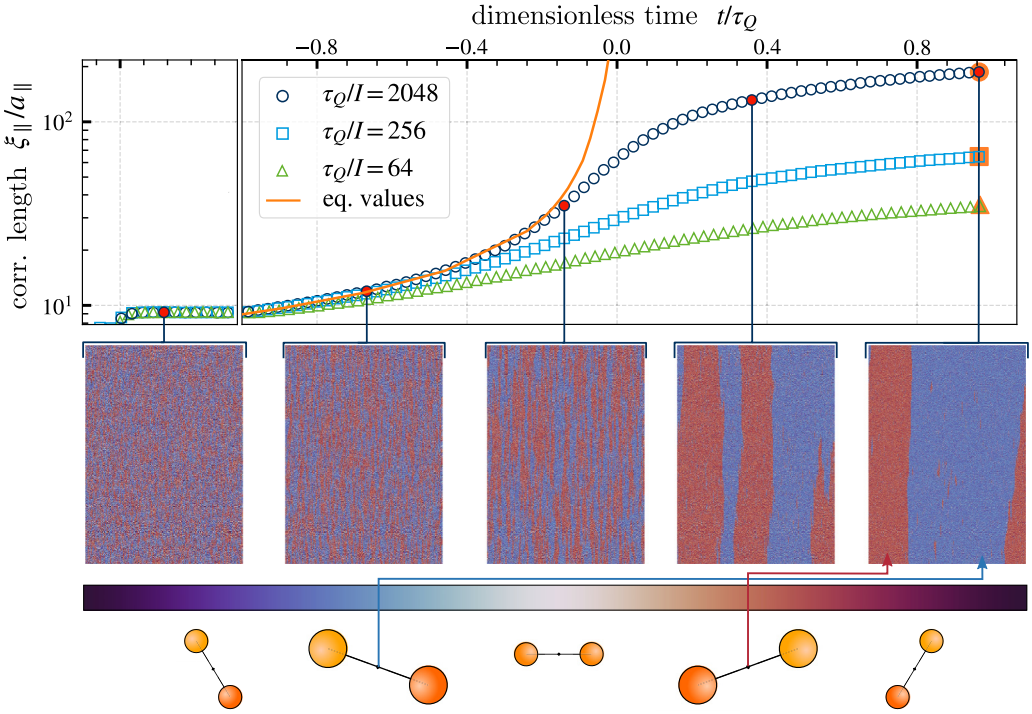

FIG. 6. The time-resolved parallel correlation length $\xi_\parallel(t)$ is shown for quenches of different timescales in the top plot. The systems go through an equilibration phase before the quench starts. The orange curve depicts the equilibrium values $\xi_\parallel(\varepsilon(t))$, visualizing where the systems deviate from adiabatic evolution. For the red markers, section snapshots of one representative quenched system at the specified time are shown below. The coloring of the meshes maps into the dimer angle and is depicted by the cyclic colorbar on the bottom. In the frozen state after the quench, the majority of dimers are in one of the equilibrium buckling states. The final quench values are highlighted as orange symbols. They can be found again in Fig. 7.

exponents while neglecting the $\eta = 0.01$ case is sensible. We extract

$$\mu_Q = 0.45. \tag{21}$$

The statistical uncertainty calculated as the standard error of Fig. 7 is less than 0.01 and also expected to be smaller than the systematic error. An explanation for the deviation to Eq. (7) might be found in the so-called quench angle,

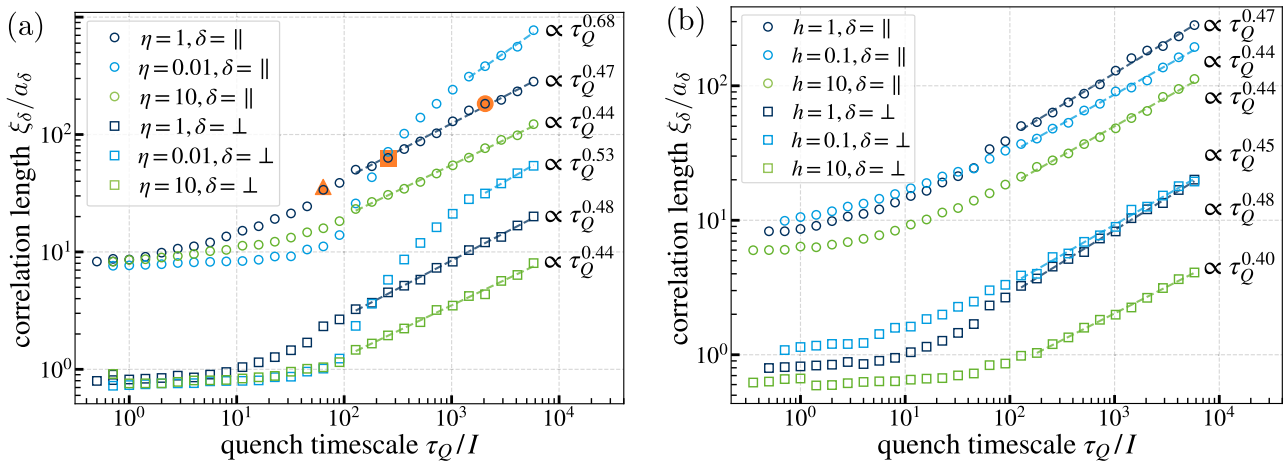

FIG. 7. The quench scaling, i.e., the frozen correlation length after a cooling quench vs the quench timescale, is shown. The data points corresponding to the final values of Fig. 6 are highlighted in the left panel. For rapid quench rates, the system is unable to evolve adiabatically from the outset. The resulting frozen correlation length corresponds approximately to the equilibrium correlation length at the initial temperature, and no scaling behavior is observed. Hence, the scaling is calculated in the linear area. The extracted quench exponents of $\mu_Q^\parallel = 0.47$ and of $\mu_Q^\perp = 0.48$ are larger than the expected $\mu_{\mathrm{KZM}} \approx 0.32$ for the Ising model. The quench scaling is simulated for systems with varying η and h in panels (a) and (b), respectively. Unlike the damping η which solely influences the dynamics, the field strength h shifts the critical point (see Fig. 10) and therefore alters the quenched temperature range. In addition for the cases with small damping, where a bump in the scaling region becomes visible, the quench exponent does not show a clear systematic dependence.

defined in Appendix D, which has been introduced in [81] and [82]. As our system is quenched, it traces a certain path in the three-dimensional phase space spanned by the effective coupling constants. Depending on the quantitative values of the coupling parameters and the quench protocol, the path crosses the phase boundary at a certain angle. This quench angle and the velocity at which the critical point is crossed open up subleading scaling regimes with $\mu_Q > \nu/(1+\nu z)$ that are dictated by the irrelevant exponents: The KZM scaling is obtained for very slow quenches or orthogonal quench angles. Further research is required to confirm or deny this hypothesis.

Previously, some of us have simulated [12] the quench with the Ising model, for which a quench exponent of $\mu_Q \approx 0.35$ much closer to Kibble-Zurek scaling was found. Additionally, the linear scaling region of $\xi_\perp$ was shifted to larger quench timescales in comparison with $\xi_\parallel$, resulting in a modification of the quenched correlation length ratio $\widehat{\xi}_\parallel/\widehat{\xi}_\perp$. This behavior is also found in the present simulation. The strongest effect is visible in the large-h curves in Fig. 7. Consequently, the ratio $\widehat{\xi}_\parallel/\widehat{\xi}_\perp$ in the scaling region increases with increasing h.

V. CONCLUSION

During this work, Langevin dynamics methods have been employed to investigate the phase transition on the Si(001) surface. The main innovation has been the step from discrete descriptions using the Ising model to a continuous formulation utilizing an adapted XY model. The purpose of the continuous description is a more realistic modeling of dynamic nonequilibrium behavior. The used Langevin equations were numerically implemented using parallel processing techniques on GPUs.

Finite-size analysis using the Binder cumulant has determined the static critical exponent ν and the dynamic exponent of the twofold symmetry-broken XY model to $\nu = 1.04$ and $z = 2.13$. Strong arguments for the validity of José *et al.*'s work [34] for rational $2 < p \leqslant 4$ have been found. Consequently, the symmetry-broken XY model with rational p is strongly expected to belong to the Ising universality class. The dynamics on the silicon surface have been studied for $J_\parallel/J_\perp = 100$. The quench exponent has been extracted to $\mu_Q = 0.45$, which is significantly larger than the expected Ising value. The influence of the amplitude of the symmetry-breaking field as well as the damping η on the quench exponent have been investigated. A dependence of μ_Q could not be established. The quench angle [81] is hypothesized as a source for the deviation between KZM scaling and the observed scaling.

However, the reason for the deviation is uncertain at the moment. The measurement of as-slow-as-possible quenches might be a starting point for further investigations, although from the current point of view, more than ten times slower quenches will not be realizable. If the deviation from the KZM exponent is caused by the subleading scalings described in [81,82], another approach could be to quench orthogonally to the phase boundary. The expected KZM scaling should then be observed also for shorter quench times. However, it is not trivial to construct an orthogonal quench protocol because the relevant couplings, that might be combinations of naive βJ_δ, βh, have to be determined first. An insightful extension to the simulation would be to allow nonlinear and anisotropic quenches. According to [81], nonlinear quench protocols of higher order $\gamma \in \mathbb{N}$ following $\varepsilon(t) = t^\gamma/\tau_Q^\gamma$ might activate scaling regions governed by the smallest irrelevant exponents. This could give valuable hints about the deviations from KZM scaling that we observe. Anisotropic quenches might be relevant for experimental systems in which the temperature of the bath and the surface is not perfectly isotropic. Another interesting avenue of further research is the investigation of the parameter p. As long as $p \in (2, 4]$, so that the number of minima of the symmetry-breaking field stays the same, it is not expected that the critical behavior changes. However, since it changes the height of the barrier, p is going to have a quantitative influence. Nevertheless, the study of the influence of p on the dynamics might be worthwhile, since the parameter also alters the shape of the symmetry-breaking field.

To conclude, the investigation of the anisotropic XY model with rational p by Langevin dynamics simulations gives a first confirmation of the Ising-like dynamic critical exponent z. The investigation of cooling quenches showed nonuniversal behavior, possibly related to the damping or the quench angle.

ACKNOWLEDGMENT

We thank P. Kratzer for fruitful discussion. We also thank the DPG for funding through the Collaborative Research Center 278162697-SFB 1242.

APPENDIX A: NUMERICS

1. Integration method

Many integration schemes have been developed to solve Eqs. (12), each with their own advantages [83]. The Brünger-Brooks-Karplus (BBK) method integrates in three steps [84]: a half-kick (we omit indices for brevity)

$$\omega\left(t+\tfrac{1}{2}\mathrm{d}t\right) = \left(1-\tfrac{1}{2}\eta\mathrm{d}t\right)\omega(t) - \tfrac{1}{2}\mathrm{d}t\,\tfrac{\partial V(\vartheta(t))}{\partial\vartheta} + \tfrac{1}{2}\sqrt{2\eta k_B T}\,n(t)\sqrt{\mathrm{d}t} \tag{A1}$$

is followed by a drift

$$\vartheta(t+\mathrm{d}t) = \vartheta(t) + \omega\left(t+\tfrac{1}{2}\mathrm{d}t\right)\mathrm{d}t, \tag{A2}$$

which is followed by another half-kick

$$\omega(t+\mathrm{d}t) = \left(1+\tfrac{\mathrm{d}t}{2}\eta\right)^{-1}\Big(\omega(t+\tfrac{\mathrm{d}t}{2}) - \tfrac{1}{2}\mathrm{d}t\,\tfrac{\partial V(\vartheta(t+\mathrm{d}t))}{\partial\vartheta} + \tfrac{1}{2}\sqrt{2\eta k_B T}\,n(t+\mathrm{d}t)\sqrt{\mathrm{d}t}\Big). \tag{A3}$$

Here, the variable $n(t)$ is a sample value of a Gaussian normal distribution with mean zero and unit standard deviation. The moment of inertia I has been set to 1. The GPU implementation makes use of the fact that the calculations Eqs. (A1)–(A3) on each lattice site can be simultaneously performed in real time, allowing much larger systems to be simulated. Inspired by Ahnert *et al.*'s architecture of solving differential equations on GPUs [85], our implementation has been extended to accommodate stochastic differential equations. The random numbers $n(t)$ have been generated using CUDA's built-in library cuRAND.

2. Benchmarks

Since an analytic solution of our model is intractable, proper benchmarks are vital to ensure the correctness of our simulation. Furthermore, the step size $\mathrm{d}t$ used to integrate the Langevin equations has to be analyzed to ensure convergence as well as avoiding discretization errors while being efficient. The benchmarks that were conducted are the dynamics of independent harmonic oscillators coupled to a thermal reservoir, and the equilibrium distribution of particle pairs described by a Hamiltonian analogous to Eq. (11). The equation that describes the time evolution of probability densities of Brownian motion is the *Fokker-Planck equation*. When talking about the probability density $p(x, v, t)$ in terms of particle velocity v and position x, it is often referred to as the *Klein-Kramers-* or *Smoluchowski* equation and written as

$$\frac{\partial}{\partial t}p(x,v,t) = \left(-\frac{\partial}{\partial x}v + \frac{\partial}{\partial v}\left[\eta v - \frac{1}{m}\frac{\partial}{\partial x}V(x)\right] + \frac{\eta k_B T}{m}\frac{\partial}{\partial v^2}\right)p(x,v,t). \tag{A4}$$

The Fokker-Planck equation and the Langevin Eqs. (12) are equivalent [63]. The distribution of paths following Langevin equations results in the probability distribution satisfying Eq. (A4). The steady-state distribution of the Fokker-Planck equation is the canonical distribution

$$p(x,v) \propto e^{-\beta\left(\frac{1}{2}mv^2 + V(x)\right)}, \tag{A5}$$

allowing for a simple way to verify long-term behavior.

For uncoupled harmonic oscillators subject to a quadratic potential

$$V(x) = \tfrac{1}{2}\omega^2 x^2, \tag{A6}$$

the Fokker-Planck equation is analytically solvable [63]. This makes it suitable to check correct dynamics of the simulation. The analytic solution for the second moment of $x(t)$ reads

$$\langle x^2\rangle(t) = \frac{\eta k_B T}{m(\lambda_+ - \lambda_-)^2}\left[\frac{\lambda_+ + \lambda_-}{\lambda_+\lambda_-} + \frac{4}{\lambda_+ + \lambda_-}\left(e^{-(\lambda_+ + \lambda_-)t} - 1\right) - \frac{1}{\lambda_+}e^{-2\lambda_+ t} - \frac{1}{\lambda_-}e^{-2\lambda_- t}\right], \tag{A7}$$

with

$$\lambda_\pm = \frac{1}{2}(\eta \pm \sqrt{\eta^2 - 4\omega^2}). \tag{A8}$$

In Fig. 8 we compare $\langle x^2\rangle(t)$ calculated from 10^5 paths, simulated by the BBK method, with the theoretical result. The algorithm with $\mathrm{d}t = 0.05$ yields small deviations from the theoretical curve. For a smaller step size of $\mathrm{d}t = 0.01$, the accuracy of the method for thermal oscillators is much better.

The second benchmark, consisting of two interacting particles in a cosine potential, has the purpose of verifying the correct behavior of the interaction as well as thermalization. We consider the one-dimensional version of Eq. (11) for two sites, so particle pairs in a cosine potential interacting via an

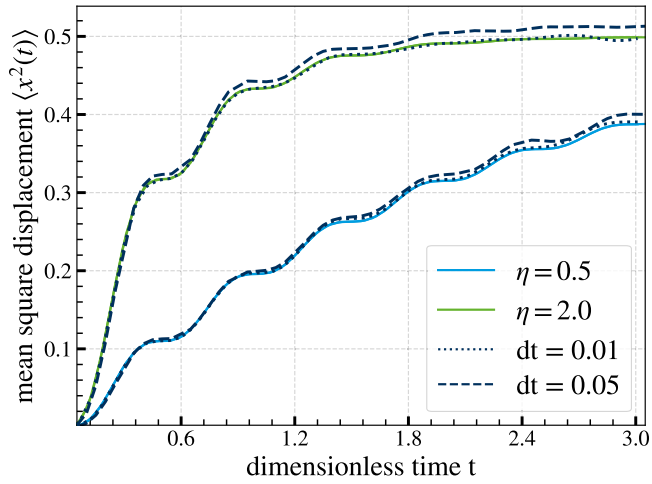

FIG. 8. The calculated $\langle x^2(t)\rangle$ of thermal harmonic oscillators are shown for two step sizes. The solid curves are the theoretical paths calculated from Eq. (A7) for $\omega^2 = 20$, $T = 20$, and $m = 1$. The damping is denoted in the legend. The dotted lines are paths calculated from 10^5 simulated trajectories. The BBK method in this use case is very stable and shows only small discretization errors up to a step size of $\mathrm{d}t = 0.05$. For a step size of $\mathrm{d}t = 0.01$, virtually no discretization errors occur.

XY interaction. Analogous to the actual simulation, the state space is restricted to $\vartheta \in [-\pi/2, \pi/2)$ and the potential is chosen as in Fig. 3(b). The probability distribution becomes a four-dimensional function $p(\vartheta_1, \vartheta_2, \omega_1, \omega_2)$. We expect that this distribution relaxes to the equilibrium distribution of the Fokker-Planck equation, i.e., the canonical distribution.

A suitable representation is achieved by integrating out the angular velocities and considering a cross section of a fixed interval $[\vartheta_2 - \frac{1}{2}\Delta\vartheta_2, \vartheta_2 + \frac{1}{2}\Delta\vartheta_2]$. In Fig. 9, we show cross sections of the integrated probability density

$$p(\vartheta_1, \vartheta_2)\Delta\vartheta_2 = \int \mathrm{d}\omega_1\, \mathrm{d}\omega_2\, p(\vartheta_1, \vartheta_2, \omega_1, \omega_2)\Delta\vartheta_2, \tag{A9}$$

with constant ϑ_2. It is verified that simple interacting systems are driven to their thermal equilibrium. The statistical and discretization errors vanish for many samples and small step sizes $\mathrm{d}t$.

APPENDIX B: EXTRACTION OF OBSERVABLES

The observables of interest are usually obtained by *ensemble averages* of systems in thermal equilibrium. The ensemble average is calculated by computing the desired observable for many different realizations of the same system. The *ergodic hypothesis* assumes that the average of many realizations and the average over one long-term simulation are the same. We assume that our system is ergodic. Since GPU accelerated programming is employed, we want to harness the full potential of the graphical processing unit. Systems of sufficient scale should be simulated to optimize GPU usage. Depending on the GPU, maximum performance is usually acquired by using systems with more than $N = 5 \times 10^5 \cdots 1 \times 10^6$ lattice sites. For many use cases, e.g., calculating the Binder cumulant U in Sec. IV A, systems of this size are not required. Therefore,

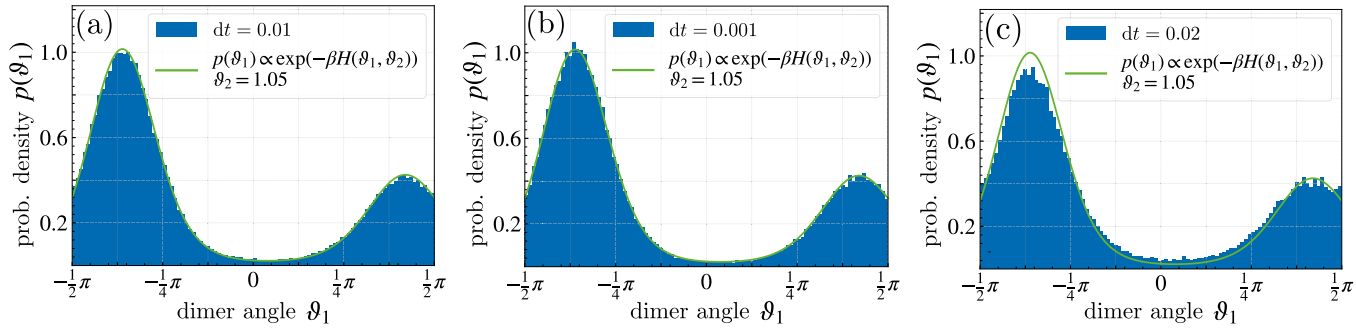

FIG. 9. The integrated probability distribution $p(\vartheta_1) = p(\vartheta_1, \vartheta_2 = 1.05)\Delta\vartheta_2$ of particle pairs described by Eq. (9) around constant ϑ_2 with $\Delta\vartheta_2 = 0.15$ is shown. The used parameters for (a)–(c) were $J = 40/I$, $h = 100/I$, $p = 2.5$, $\eta = 1$, and $T = 100/I$. The interactions and temperatures are chosen to be larger than in the actual simulation on purpose. The green curve is the canonical distribution. The blue bins are calculated from 5×10^5 simulated pair paths by counting particles in $[\vartheta_2 - \frac{1}{2}\Delta\vartheta_2, \vartheta_2 + \frac{1}{2}\Delta\vartheta_2]$ and binning them into 100 sections for ϑ_1. It was made sure that the systems were completely relaxed, meaning that the effects of the starting position vanished, and the shape of the probability distribution was stable. The BBK method again shows no discretization errors for $dt = 0.01$. Slightly larger step sizes of $dt = 0.02$ already produce visually recognizable deviations. Almost no improvement is achieved by reducing the step size to $dt = 0.001$.

always a number $n \approx N/(L_\parallel L_\perp)$ of independent subsystems is simulated. For a simulation of n subsystems over a time τ_s, the ensemble average of a quantity f is calculated via

$$\langle f \rangle = \frac{1}{n\tau_s} \sum_i^n \int_{t_0}^{t_0+\tau_s} ds f_i(s). \tag{B1}$$

To calculate the Binder cumulant Eq. (15), the ensemble averages of $f = M^2$ and M^4 have to be evaluated. In the case of the correlation length extraction relevant in Sec. IV C and described in Appendix C, the Fourier transform (C5) of the correlation function $S_\delta(k)$ is calculated as the summed squares of the lattice Fourier transform (C11) and averaged before fitting Eq. (C12). For the time-dependent Binder cumulant $U(t, \varepsilon, L)$ of Sec. IV B, the time integration in Eq. (B1) is restricted to an interval $s \in [t - \frac{d\sigma}{2}, t + \frac{d\sigma}{2})$ with the step size $d\sigma$ chosen for suitable representation. The averaging process is repeated until major fluctuations have averaged out. When making use of the ergodic hypothesis to calculate equilibrium quantities, like in Fig. 4 or the orange curve in Fig. 6, it is important to make sure that the system is actually thermalized. Usually, a lower time bound t_0 is introduced to account for the relaxation time. Again, the relaxation time is not known, and therefore t_0 is set to a fraction of τ_s to eliminate strong fluctuations in the equilibration phase of the simulation. To eventually judge the relaxation of the system, the uncertainty of $\langle f \rangle$ is considered. The approach is that the equilibration introduces a large statistical deviation on the average $\langle f \rangle$. So by calculating the error $\Delta\langle f \rangle$, we can extract information about the state of equilibration of the system. The $f_i(s)$ are correlated for different points in time. The strength of the correlation depends on how quickly the system relaxes. To get reasonable estimates on the error of $\langle f \rangle$, we have to judge how many effectively independent readings of f_i are taken by the ds integration in Eq. (B1). Analyzing $f_i(s)$ as time series helps to avoid terminating the simulation too early for slowly relaxing systems. Additionally, it gives an estimate for how many measurements should be recorded in order not to overflow with data.

On the run, $f_i(s)$ is calculated and saved for discrete time steps ds. The sample time step ds is usually much larger than the integration step size

$$ds \gtrsim 100 \times dt \tag{B2}$$

to limit the amount of data generation. The exact value depends on the integrated autocorrelation time τ_C (B7) and is adapted during the simulation,

$$ds \approx \frac{1}{10}\tau_C. \tag{B3}$$

An average that is calculated by means of Eq. (B1) has a nontrivial relationship with its variance [86]. The reason for this is that $f_i(s)$ and $f_i(s + ds)$ can be correlated. Observables at different points in time are dependent on each other and have to be treated accordingly. The average f_{τ_s} of a time series $f(s)$ (omit indices for brevity) is calculated as

$$f_{\tau_s} = \frac{1}{\tau_s} \int_0^{\tau_s} ds f(s), \tag{B4}$$

with τ_s being the duration of the sampling. To estimate the error on f_{τ_s}, we consider its variance [30,87]

$$\begin{aligned} \sigma^2_{f_{\tau_s}} &= \langle f^2_{\tau_s} \rangle - \langle f_{\tau_s} \rangle^2 \\ &\approx \frac{1}{\tau_s} \int_{-\infty}^{\infty} dt\, C_f(t), \end{aligned} \tag{B5}$$

with $C_f(t)$ being the autocorrelation or time correlation function

$$C_f(t) = \lim_{s\to\infty} (\langle f(s) f(s+t) \rangle - \langle f(s) \rangle^2). \tag{B6}$$

The step performed in Eq. (B5) is valid in the limit that the sampling time is much larger than the characteristic decay time of the autocorrelation function τ_C. The so-called *integrated autocorrelation time* τ_C is defined as

$$\tau_C = \frac{1}{2} \int_{-\infty}^{\infty} dt\, C_f(t)/C_f(0). \tag{B7}$$

The variance $\sigma^2_{f_{\tau_s}}$ is expressed in terms of τ_C as

$$\sigma^2_{f_{\tau_s}} = \frac{2\tau_C}{\tau_s} C_f(0). \tag{B8}$$

Consideration of Eq. (B6) shows that $C_f(0)$ reduces to the variance of f,

$$C_f(0) = \sigma_f^2. \tag{B9}$$

Rewriting $\tau_s = n_s \Delta s$ with n_s being the number of measured samples and $\mathrm{d}s \to \Delta s$ being the discrete time between the samples, the variance of the mean f_{τ_s} can be expressed as

$$\sigma^2_{f_{\tau_s}} = \frac{2\tau_C}{\tau_s}\sigma_f^2 = \frac{2\tau_C}{\Delta s}\frac{\sigma_f^2}{n_s}, \tag{B10}$$

revealing that the variance of f_{τ_s} is larger by a factor of $2\tau_c/\Delta s$ than the naive approach of uncorrelated measurements. Since it is practically not possible to integrate Eq. (B7) from $-\infty$ to ∞, we approximate τ_c by

$$\tau_C \approx \frac{1}{2}\int_{-\tau_s/2}^{\tau_s/2} \mathrm{d}t\, C_f(t)/C_f(0). \tag{B11}$$

APPENDIX C: CORRELATION LENGTH EXTRACTION

The two-point equal-time correlation function of the XY model with rotors $\vec{s}_{x,y} = (\cos\vartheta_{x,y}, \sin\vartheta_{x,y})$ in two dimensions is defined as

$$C(x, y) = \langle \vec{s}_{0,0}\vec{s}_{x,y}\rangle. \tag{C1}$$

The brackets $\langle\cdot\rangle$ denote the ensemble average

$$\langle \vec{s}_{0,0}\vec{s}_{x,y}\rangle = \frac{1}{Z}\int \prod_i d\vartheta_i \vec{s}_{0,0}\vec{s}_{x,y} e^{-\beta H(\{\vartheta\})}. \tag{C2}$$

The correlation function decays exponentially for large distances above the critical temperature [33,35], following

$$C(x, y) \sim e^{-r(x,y)/\xi(x,y)} \quad \text{with} \quad r(x, y) = \sqrt{x^2 + y^2}. \tag{C3}$$

This is the definition of the correlation length ξ. The correlation length is a measure for the lengthscale over which perturbations of a system relax in space. We are mainly interested in the correlation lengths in the directions along and across the dimer row and therefore define the correlation functions in these directions as

$$\begin{aligned} C_\perp(y) &= \langle \vec{s}_{0,0}\vec{s}_{0,y}\rangle \sim e^{-y/\xi_\perp} \quad \text{and} \\ C_\parallel(x) &= \langle \vec{s}_{0,0}\vec{s}_{x,0}\rangle \sim e^{-x/\xi_\parallel}. \end{aligned} \tag{C4}$$

Consider the Fourier transforms of $C_\delta(r)$, $\delta \in \{\parallel, \perp\}$,

$$S_\delta(k) = \sum_{r=0}^{N_\delta - 1} C_\delta(r) e^{-2\pi \mathrm{i}\frac{kr}{N_\delta}}, \tag{C5}$$

with N_δ being the number of lattice sites in the direction of δ. Set in the following, $\delta = \perp$. The Fourier transform becomes

$$\begin{aligned} S_\perp(k) &= \sum_{y=0}^{N_\perp - 1} C_\perp(y) e^{-2\pi \mathrm{i}\frac{ky}{N_\perp}} = \sum_{y=0}^{N_\perp - 1} \langle \vec{s}_{0,0}\vec{s}_{0,y}\rangle e^{-2\pi \mathrm{i}\frac{ky}{N_\perp}} \\ &= \sum_{\kappa=0}^{1}\sum_{y=0}^{N_\perp - 1} \langle s^\kappa_{0,0} s^\kappa_{0,y}\rangle e^{-2\pi \mathrm{i}\frac{ky}{N_\perp}}, \end{aligned} \tag{C6}$$

with $\kappa \in \{0, 1\}$ denoting the spin component. The ensemble average can be computed by a sum over an infinite lattice,

$$\langle s^\kappa_{0,0} s^\kappa_{0,y}\rangle = \lim_{N_\perp\to\infty}\lim_{N_\parallel\to\infty} \frac{1}{N_\perp N_\parallel}\sum_{i=0}^{N_\perp}\sum_{j=0}^{N_\parallel} s^\kappa_{i,j} s^\kappa_{i,j+y}. \tag{C7}$$

An approximation is possible by using a finite lattice with large dimensions N_δ. Inserting Eq. (C7) into Eq. (C6) and replacing $j + y \to q$ yields

$$\begin{aligned} S_\perp(k) &= \frac{1}{N_\perp N_\parallel}\sum_{\kappa,q,i,j} s^\kappa_{i,j} s^\kappa_{i,q} e^{-2\pi \mathrm{i}\frac{k(q-j)}{N_\perp}} \\ &= \frac{1}{N_\perp N_\parallel}\sum_{\kappa,q,i,j}\left(\sum_{p=0}^{N_\parallel}\delta_{i,p}\right) s^\kappa_{i,j} s^\kappa_{p,q} e^{-2\pi \mathrm{i}\frac{k(q-j)}{N_\perp}}. \end{aligned} \tag{C8}$$

In the second step, we have inserted an identity in the form of a sum over a Kronecker δ. The Kronecker δ can be written as a sum over complex exponentials,

$$\delta_{p,j} = \frac{1}{N_\parallel}\sum_{l=1}^{N_\parallel} e^{2\pi \mathrm{i}\frac{l(j-p)}{N_\parallel}}. \tag{C9}$$

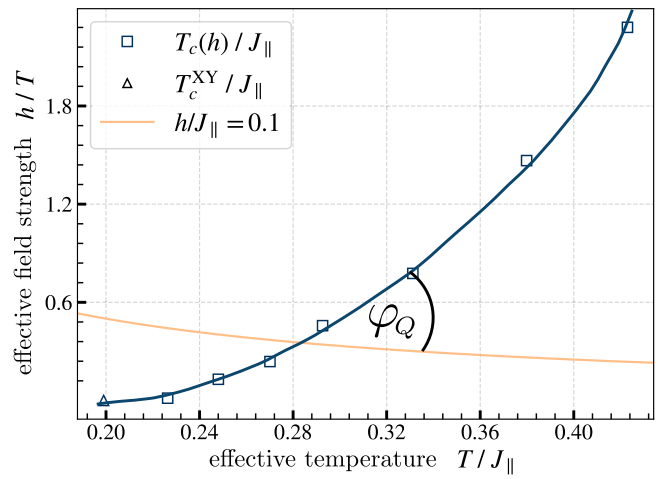

FIG. 10. Some simulated critical points are shown for the adapted XY model with $J_\parallel/J_\perp \approx 30$. We added a guide for the eye for the phase boundary. The triangle marks the Kosterlitz-Thouless transition of the XY model without a symmetry-breaking field calculated by an approximation [88]. A system with constant couplings traces a path (orange) in the phase space when cooled down. The path crosses the phase boundary at an angle φ_Q, in this work called the quench angle. In [81,82] it has been reported that steep quench angles and fast quenches open up subleading scaling regimes that are dictated by irrelevant exponents.

Inserting this representation into Eq. (C8) gives

$$S_\perp(k) = \frac{1}{N_\perp N_\parallel^2} \sum_l \sum_\kappa \sum_{q,p,i,j} s^\kappa_{i,j} s^\kappa_{p,q} e^{-2\pi \mathrm{i} \frac{k(q-j)}{N_\perp}} e^{2\pi \mathrm{i} \frac{l(p-i)}{N_\parallel}}$$
$$= \frac{1}{N_\perp N_\parallel^2} \sum_l \sum_\kappa \left(\sum_{i,j} s^\kappa_{i,j} e^{2\pi \mathrm{i} \left(\frac{kj}{N_\perp} + \frac{li}{N_\parallel} \right)} \right)$$
$$\times \left(\sum_{q,p} s^\kappa_{p,q} e^{-2\pi \mathrm{i} \left(\frac{kq}{N_\perp} + \frac{lp}{N_\parallel} \right)} \right). \tag{C10}$$

The expressions in the parentheses are the Fourier transforms $\tilde{s}^\kappa_{k,l}$, or, respectively, the conjugated Fourier transform, of the lattice $s^\kappa_{i,j}$:

$$S_\perp(k) = \frac{1}{N_\perp N_\parallel^2} \sum_l \sum_\kappa \left(\tilde{s}^\kappa_{k,l} \right)^* \tilde{s}^\kappa_{k,l}$$
$$= \frac{1}{N_\perp N_\parallel^2} \left(\sum_l \left| \tilde{s}^0_{k,l} \right|^2 + \sum_l \left| \tilde{s}^1_{k,l} \right|^2 \right). \tag{C11}$$

This way we can calculate $S_\perp(k)$ by computing the two-dimensional Fourier transforms of the lattices $s^0_{i,j} = \cos \vartheta_{i,j}$ and $s^1_{i,j} = \sin \vartheta_{i,j}$. The analog result is valid for $S_\parallel(k)$.

To eventually extract the correlation length, we consider again Eq. (C8) and insert the asymptotic behavior of $C_\delta(r)$ [Eq. (C4)] to obtain

$$S_\delta(k) \sim \sum_r^{N_\delta - 1} e^{-|r|/\xi_\delta} e^{-2\pi \mathrm{i} \frac{kr}{N_\delta}} = \frac{2\xi_\delta}{1 + 4\pi^2 \xi_\delta^2 k^2}, \tag{C12}$$

showing that $S_\delta(k)$ behaves like a Lorentzian function around $k = 0$. Calculating $S_\delta(k)$ by means of Eq. (C11) and fitting to the Lorentzian Eq. (C12) yields ξ_δ as a fitting parameter. Since Eq. (C3) is valid for large r, it is important to only fit the peak of $S_\delta(k)$ around $k = 0$. Correlations below the critical temperature in the Ising universality class can be shown [42] to decay like

$$C(x, y) \sim c + e^{-r(x,y)/\xi(x,y)}, \tag{C13}$$

with a positive constant c. When performing the Fourier transform, this constant contributes to a δ peak at $k = 0$. To correctly extract correlation lengths below T_c, the $S_\delta(k = 0)$ value has to be cut.

APPENDIX D: PHASE DIAGRAM

The critical point of the symmetry-broken XY model depends on the field strength h. A cross section of the phase space in the $\beta h - (\beta J_\parallel)^{-1}$ plane is shown in Fig. 10. When reducing the temperature while keeping the couplings constant, the system traces a path in the phase space and crosses the phase boundary at the critical temperature. We call the angle between the path and the phase boundary *quench angle*.

APPENDIX E: ISING DYNAMIC CRITICAL EXPONENT

The anisotropic Ising model is part of *Model A* as specified by Hohenberg and Halperin [39]. Its dynamic critical exponent z can be expressed in terms of

$$z = 2 + c\tilde{\eta} \tag{E1}$$

with the known critical exponent $\tilde{\eta}$ and a constant c to be determined. Some recent results of z are given in Table I.

[1] J. Dabrowski *et al.*, *Silicon Surfaces and Formation of Interfaces: Basic Science in the Industrial World* (World Scientific, Singapore, 2000).

[2] A. Ramstad, G. Brocks, and P. J. Kelly, Theoretical study of the Si(100) surface reconstruction, Phys. Rev. B **51**, 14504 (1995).

[3] D. Pillay, B. Stewart, C. B. Shin, and G. S. Hwang, Revisit to the Ising model for order–disorder phase transition on Si(001), Surf. Sci. **554**, 150 (2004).

[4] K. Inoue, Y. Morikawa, K. Terakura, and M. Nakayama, Order-disorder phase transition on the Si(001) surface: Critical role of dimer defects, Phys. Rev. B **49**, 14774 (1994).

[5] J. Ihm, D. H. Lee, J. D. Joannopoulos, and J. J. Xiong, Structural phase diagrams for the surface of a solid: a total-energy, renormalization-group approach, Phys. Rev. Lett. **51**, 1872 (1983).

[6] C. Fu, M. Weissmann, and A. Saúl, Molecular dynamics study of dimer flipping on perfect and defective Si(001) surfaces, Surf. Sci. **494**, 119 (2001).

[7] M. Matsumoto, K. Fukutani, and T. Okano, Low-energy electron diffraction study of the phase transition of Si(001) surface below 40 K, Phys. Rev. Lett. **90**, 106103 (2003).

[8] M. Kubota and Y. Murata, Streak patterns in low-energy electron diffraction on Si(001), Phys. Rev. B **49**, 4810 (1994).

[9] C. Brand, A. Hucht, H. Mehdipour, G. Jnawali, J. D. Fortmann, M. Tajik, R. Hild, B. Sothmann, P. Kratzer, R. Schützhold *et al.*, Critical behavior of the dimerized Si(001) surface: Continuous order-disorder phase transition in the two-dimensional Ising universality class, Phys. Rev. B **109**, 134104 (2024).

[10] R. A. Wolkow, Direct observation of an increase in buckled dimers on Si(001) at low temperature, Phys. Rev. Lett. **68**, 2636 (1992).

[11] H. Tochihara, T. Amakusa, and M. Iwatsuki, Low-temperature scanning-tunneling-microscopy observations of the Si(001) surface with a low surface-defect density, Phys. Rev. B **50**, 12262 (1994).

[12] G. Schaller, F. Queisser, S. P. Katoorani, C. Brand, C. Kohlfürst, M. R. Freeman, A. Hucht, P. Kratzer, B. Sothmann, M. Horn-von Hoegen *et al.*, Sequential Kibble-Zurek dynamics in the anisotropic Ising model of the Si (001) surface, arXiv:2310.18216.

[13] T. Tabata, T. Aruga, and Y. Murata, Order-disorder transition on Si(001): c(4 × 2) to (2 × 1), Surf. Sci. Lett. **179**, L63 (1987).

[14] T. W. B. Kibble, Topology of cosmic domains and strings, J. Phys. A **9**, 1387 (1976).

[15] W. H. Zurek, Cosmological experiments in superfluid helium? Nature (London) **317**, 505 (1985).
[16] W. H. Zurek, Cosmological experiments in condensed matter systems, Phys. Rep. **276**, 177 (1996).
[17] V. M. H. Ruutu, V. B. Eltsov, A. J. Gill, T. W. B. Kibble, M. Krusius, Y. G. Makhlin, B. Placais, G. E. Volovik, and W. Xu, Vortex formation in neutron-irradiated superfluid ^{3}He as an analogue of cosmological defect formation, Nature (London) **382**, 334 (1996).
[18] S. Ulm, J. Roßnagel, G. Jacob, C. Degünther, S. T. Dawkins, U. G. Poschinger, R. Nigmatullin, A. Retzker, M. B. Plenio, F. Schmidt-Kaler *et al.*, Observation of the Kibble–Zurek scaling law for defect formation in ion crystals, Nat. Commun. **4**, 2290 (2013).
[19] K. Pyka, J. Keller, H. L. Partner, R. Nigmatullin, T. Burgermeister, D. M. Meier, K. Kuhlmann, A. Retzker, M. B. Plenio, W. H. Zurek *et al.*, Topological defect formation and spontaneous symmetry breaking in ion Coulomb crystals, Nat. Commun. **4**, 2291 (2013).
[20] P. Laguna and W. H. Zurek, Density of kinks after a quench: When symmetry breaks, how big are the pieces? Phys. Rev. Lett. **78**, 2519 (1997).
[21] N. D. Antunes, P. Gandra, and R. J. Rivers, Is domain formation decided before or after the transition? Phys. Rev. D **73**, 125003 (2006).
[22] C. Bäuerle, Y. M. Bunkov, S. N. Fisher, H. Godfrin, and G. R. Pickett, Laboratory simulation of cosmic string formation in the early Universe using superfluid ^3He, Nature (London) **382**, 332 (1996).
[23] V. B. Eltsov, M. Krusius, and G. E. Volovik, Vortex formation and dynamics in superfluid ^{3}He and analogies in quantum field theory, Prog. Low Temp. Phys. **15**, 1 (2005).
[24] G. E. Volovik, *The Universe in a Helium Droplet* (Oxford University Press, Oxford, 2003), Vol. 117.
[25] Y. M. Bunkov, A. I. Golov, V. S. L'vov, A. Pomyalov, and I. Procaccia, Evolution of a neutron-initiated micro big bang in superfluid ^{3}He–*B*, Phys. Rev. B **90**, 024508 (2014).
[26] F. J. Himpsel and D. E. Eastman, Photoemission studies of intrinsic surface states on Si(100), J. Vac. Sci. Technol. **16**, 1297 (1979).
[27] R. I. G. Uhrberg, G. V. Hansson, J. M. Nicholls, and S. A. Flodström, Experimental studies of the dangling-and dimer-bond-related surface electron bands on Si(100) (2×1), Phys. Rev. B **24**, 4684 (1981).
[28] K. Handa, S. Kono, K. Saku, J. Sasaki, T. Kawano, Y. Sasaki, T. Hiroki, and K. Arakawa, Plasma fibrinogen levels as an independent indicator of severity of coronary atherosclerosis, Atherosclerosis **77**, 209 (1989).
[29] D. T. Gillespie, The mathematics of Brownian motion and Johnson noise, Am. J. Phys. **64**, 225 (1996).
[30] D. Frenkel and B. Smit, *Understanding Molecular Simulation: From Algorithms to Applications* (Elsevier, Amsterdam, 2023).
[31] K. Du, X. Fang, C. Won, C. De, F.-T. Huang, W. Xu, H. You, F. J. Gómez-Ruiz, A. del Campo, and S.-W. Cheong, Kibble-Zurek mechanism of Ising domains, Nat. Phys. **19**, 1495 (2023).
[32] J. M. Kosterlitz, Kosterlitz–Thouless physics: a review of key issues, Rep. Prog. Phys. **79**, 026001 (2016).
[33] J. M. Kosterlitz, The critical properties of the two-dimensional XY model, J. Phys. C **7**, 1046 (1974).
[34] J. V. José, L. P. Kadanoff, S. Kirkpatrick, and D. R. Nelson, Renormalization, vortices, and symmetry-breaking perturbations in the two-dimensional planar model, Phys. Rev. B **16**, 1217 (1977).
[35] S. Grinstein, Spin-wave theory for the biaxial (m = 2) Lifshitz point problem in three dimensions, J. Phys. A **13**, L201 (1980).
[36] E. Barouch, B. M. McCoy, and M. Dresden, Statistical mechanics of the XY model. I, Phys. Rev. A **2**, 1075 (1970).
[37] N. Goldenfeld, *Lectures on Phase Transitions and the Renormalization Group* (CRC, Boca Raton, FL, 2018).
[38] A. Pelissetto and E. Vicari, Critical phenomena and renormalization-group theory, Phys. Rep. **368**, 549 (2002).
[39] P. C. Hohenberg and B. I. Halperin, Theory of dynamic critical phenomena, Rev. Mod. Phys. **49**, 435 (1977).
[40] B. I. Halperin and P. C. Hohenberg, Scaling laws for dynamic critical phenomena, Phys. Rev. **177**, 952 (1969).
[41] L. Onsager, Crystal statistics. I. A two-dimensional model with an order-disorder transition, Phys. Rev. **65**, 117 (1944).
[42] B. M. McCoy and T. T. Wu, *The Two-dimensional Ising Model* (Harvard University Press, Cambridge, MA, 1973).
[43] M. Hasenbusch, The two-dimensional *XY* model at the transition temperature: a high-precision Monte Carlo study, J. Phys. A **38**, 5869 (2005).
[44] W. Janke and K. Nather, High-precision Monte Carlo study of the two-dimensional *XY* villain model, Phys. Rev. B **48**, 7419 (1993).
[45] R. G. Edwards, J. Goodman, and A. D. Sokal, Multi-grid Monte Carlo (II). Two-dimensional *XY* model, Nucl. Phys. B **354**, 289 (1991).
[46] M. Kardar, *Statistical Physics of Fields* (Cambridge University Press, Cambridge, 2007).
[47] E. Lieb, T. Schultz, and D. Mattis, Two soluble models of an antiferromagnetic chain, Ann. Phys. **16**, 407 (1961).
[48] F. Pázmándi and Z. Domański, Quantum phase transitions in *XY* spin models, Phys. Rev. Lett. **74**, 2363 (1995).
[49] A. Imamoglu, D. D. Awschalom, G. Burkard, D. P. DiVincenzo, D. Loss, M. Sherwin, A. Small *et al.*, Quantum information processing using quantum dot spins and cavity QED, Phys. Rev. Lett. **83**, 4204 (1999).
[50] X. Wang, Entanglement in the quantum Heisenberg *XY* model, Phys. Rev. A **64**, 012313 (2001).
[51] K. Harada and N. Kawashima, Kosterlitz-Thouless transition of quantum *XY* model in two dimensions, J. Phys. Soc. Jpn. **67**, 2768 (1998).
[52] H.-Q. Ding and M. S. Makivić, Kosterlitz-Thouless transition in the two-dimensional quantum *XY* model, Phys. Rev. B **42**, 6827 (1990).
[53] F. C. Poderoso, J. J. Arenzon, and Y. Levin, New ordered phases in a class of generalized *XY* models, Phys. Rev. Lett. **106**, 067202 (2011).
[54] R. B. Potts, Some generalized order-disorder transformations, in *Mathematical Proceedings of the Cambridge Philosophical Society* (Cambridge University Press, Cambridge, 1952), Vol. 48, pp. 106–109.
[55] G. Attard and C. Barnes, *Surfaces, Oxford Chemistry Primers* (Oxford University Press, Oxford, 1998), p. 96.
[56] B. Mills, Wikipedia. 2024. "silicon." The silicon atoms are replaced by their own color gradients. Dimerization arrows,

coordinate system, and lattice constant added, retrieved from https://en.wikipedia.org/wiki/Silicon.
[57] D. J. Chadi, Atomic and electronic structures of reconstructed Si(100) surfaces, Phys. Rev. Lett. **43**, 43 (1979).
[58] I. P. Batra, Atomic structure of the Si(001)-(2 × 1) surface, Phys. Rev. B **41**, 5048 (1990).
[59] J. Dabrowski and M. Scheffler, Self-consistent study of the electronic and structural properties of the clean Si(001)(2 × 1) surface, Appl. Surf. Sci. **56-58**, 15 (1992).
[60] E. Landemark, C. J. Karlsson, Y.-C. Chao, and R. I. G. Uhrberg, Core-level spectroscopy of the clean Si(001) surface: Charge transfer within asymmetric dimers of the 2 × 1 and c(4 × 2) reconstructions, Phys. Rev. Lett. **69**, 1588 (1992).
[61] C. Brand, A. Hucht, G. Jnawali, J. D. Fortmann, B. Sothmann, H. Mehdipour, P. Kratzer, R. Schützhold, and M. Horn-von Hoegen, Dimer coupling energies of the Si(001) surface, Phys. Rev. Lett. **130**, 126203 (2023).
[62] A. B. Bortz, M. H. Kalos, and J. L. Lebowitz, A new algorithm for Monte Carlo simulation of Ising spin systems, J. Comput. Phys. **17**, 10 (1975).
[63] H. Risken, *Fokker-Planck Equation* (Springer, Berlin, 1996).
[64] NVIDIA, P. Vingelmann, and F. H. P. Fitzek, CUDA, release: 10.2.89 (2020), https://developer.nvidia.com/cuda-toolkit.
[65] Thrust Development Team, Thrust: The C + + parallel algorithms library, 2023.
[66] K. Binder, Monte Carlo simulations in statistical physics, in *Statistical and Nonlinear Physics* (Springer, Berlin-Heidelberg, 2022), pp. 85–97.
[67] K. W. Vugrin, L. P. Swiler, R. M. Roberts, N. J. Stucky-Mack, and S. P. Sullivan, Confidence region estimation techniques for nonlinear regression in groundwater flow: Three case studies, Water Resour. Res. **43**, 2005WR004804 (2007).
[68] C. Domb, M. S. Green, and J. L. Lebowitz, *Phase Transitions and Critical Phenomena* (Academic Press, San Diego, 1983), Vol. 8.
[69] K. Binder, Finite size scaling analysis of Ising model block distribution functions, Z. Phys. B **43**, 119 (1981).
[70] M. Campostrini, M. Hasenbusch, A. Pelissetto, P. Rossi, and E. Vicari, Critical behavior of the three-dimensional *XY* universality class, Phys. Rev. B **63**, 214503 (2001).
[71] W. Selke, Critical Binder cumulant of two-dimensional Ising models, Eur. Phys. J. B **51**, 223 (2006).
[72] K. Binder, Critical properties from Monte Carlo coarse graining and renormalization, Phys. Rev. Lett. **47**, 693 (1981).
[73] D. P. Landau, Non-universal critical behavior in the planar *XY*-model with fourth order anisotropy, J. Magn. Magn. Mater. **31-34**, 1115 (1983).
[74] W. Bernreuther and M. Göckeler, An investigation of the phase structure of the two-dimensional O(2) and O(4) symmetric nonlinear sigma-models, Phys. Lett. B **214**, 109 (1988).
[75] D. Loison, Binder's cumulant for the Kosterlitz-Thouless transition, J. Phys.: Condens. Matter **11**, L401 (1999).
[76] Z. B. Li, L. Schülke, and B. Zheng, Dynamic Monte Carlo measurement of critical exponents, Phys. Rev. Lett. **74**, 3396 (1995).
[77] M. P. Nightingale and H. W. J. Blöte, Monte Carlo computation of correlation times of independent relaxation modes at criticality, Phys. Rev. B **62**, 1089 (2000).
[78] L. T. Adzhemyan, D. A. Evdokimov, M. Hnatič, E. V. Ivanova, M. V. Kompaniets, A. Kudlis, and D. V. Zakharov, The dynamic critical exponent z for 2d and 3d Ising models from five-loop ε expansion, Phys. Lett. A **425**, 127870 (2022).
[79] C. Duclut and B. Delamotte, Frequency regulators for the nonperturbative renormalization group: A general study and the model A as a benchmark, Phys. Rev. E **95**, 012107 (2017).
[80] B. Dammann and J. D. Reger, Dynamical critical exponent of the two-dimensional Ising model, Europhys. Lett. **21**, 157 (1993).
[81] S. Mathey and S. Diehl, Activating critical exponent spectra with a slow drive, Phys. Rev. Res. **2**, 013150 (2020).
[82] B. Ladewig, S. Mathey, and S. Diehl, Kibble-Zurek mechanism from different angles: The transverse XY model and subleading scalings, Phys. Rev. B **102**, 104306 (2020).
[83] L. Larini, R. Mannella, and D. Leporini, Langevin stabilization of molecular-dynamics simulations of polymers by means of quasisymplectic algorithms, J. Chem. Phys. **126**, 104101 (2007).
[84] J. A. Izaguirre, D. P. Catarello, J. M. Wozniak, and R. D. Skeel, Langevin stabilization of molecular dynamics, J. Chem. Phys. **114**, 2090 (2001).
[85] K. Ahnert, D. Demidov, and M. Mulansky, Solving ordinary differential equations on GPUs, *Numerical Computations with GPUs* (Springer, Berlin-Heidelberg, 2014), pp. 125–157.
[86] N. Madras and A. D. Sokal, The pivot algorithm: A highly efficient Monte Carlo method for the self-avoiding walk, J. Stat. Phys. **50**, 109 (1988).
[87] T. W. Anderson, *The Statistical Analysis of Time Series* (Wiley, Hoboken, 2011), pp. 438–450.
[88] D. C. Mattis, Transfer matrix in plane-rotator model, Phys. Lett. A **104**, 357 (1984).